2012

# Hexagonal-based pyramid void defects in GaN and InGaN

A. B. Yankovich
*University of Wisconsin-Madison*

A. V. Kvit
*University of Wisconsin-Madison*

X. Li
*Virginia Commonwealth University*

***See next page for additional authors***



Yankovich, A. B., Kvit, A. V., & Li, X., et al. Hexagonal-based pyramid void defects in GaN and InGaN. Journal of Applied Physics, 111, 023517 (2012). 

# Hexagonal-based pyramid void defects in GaN and InGaN

A. B. Yankovich,[1,a)] A. V. Kvit,[1] X. Li,[2] F. Zhang,[2] V. Avrutin,[2] H. Y. Liu,[2] N. Izyumskaya,[2] Ü. Özgür,[2] H. Morkoç,[2] and P. M. Voyles[1]
[1]*Department of Materials Science and Engineering, University of Wisconsin-Madison, Madison, Wisconsin 53706, USA*
[2]*Department of Electrical and Computer Engineering, Virginia Commonwealth University, Richmond, Virginia 23284, USA*

(Received 14 September 2011; accepted 23 December 2011; published online 27 January 2012)

We report a void defect in gallium nitride (GaN) and InGaN, revealed by aberration-corrected scanning transmission electron microscopy (STEM). The voids are pyramids with symmetric hexagonal $\{0001\}$ base facets and $\{10\bar{1}1\}$ side facets. Each pyramid void has a dislocation at the peak of the pyramid, which continues up along the $[0001]$ growth direction to the surface. Some of the dislocations are hexagonal open core screw dislocations with $\{10\bar{1}0\}$ side facets, varying lateral widths, and varying degrees of hexagonal symmetry. STEM electron energy loss spectroscopy spectrum imaging showed a large C concentration inside the void and on the void surfaces. There is also a larger C concentration in the GaN (or InGaN) below the void than above the void. We propose that inadvertent carbon deposition during metal organic chemical vapor deposition growth acts as a mask, stopping the GaN deposition locally, which in combination with lateral overgrowth, creates a void. Subsequent layers of GaN deposited around the C covered region create the overhanging $\{10\bar{1}1\}$ facets, and the meeting of the six $\{10\bar{1}1\}$ facets at the pyramid's peak is not perfect, resulting in a dislocation. © *2012 American Institute of Physics*. [doi:10.1063/1.3679540]

## I. INTRODUCTION

III–nitride wide bandgap semiconductor materials are significant components in optoelectronic devices for high power, short wavelength, and high temperature applications.[1–4] Gallium nitride (GaN) and its related alloys, AlGaN and InGaN, are important in part for their role in high efficiency blue to ultraviolet light emitting diodes (LED).[5] Identifying and controlling extended defects in heteroepitaxial III–V thin films is crucial to high-power, high-current device operation, efficiency, and reliability.

GaN extended defects include threading dislocations,[6–8] stacking faults,[8] open-core dislocations,[8–11] inversion domain boundaries,[10,12] V-defects in InGaN quantum wells (QW),[13–18] and pyramid shaped inversion domains and voids in Mg-doped GaN.[19–24] Because GaN and sapphire ($Al_2O_3$), epitaxial GaN's most common substrate, are poorly matched in lattice parameter and thermal expansion coefficient, as-grown films have a high density of defects. The most common defects are threading dislocations, with typical densities of $\sim 10^{10}$ cm$^{-2}$ for molecular beam epitaxy grown films[7] and $\sim 10^{8}$ cm$^{-2}$ for metal organic chemical vapor deposition (MOCVD) films grown on $SiN_x$ nanonetworks.[25] The threading dislocations are predominantly pure edge dislocations lying along the $[0001]$ direction with a Burgers vector of $1/3\ \langle 11\bar{2}0\rangle$ created by low-angle grain boundaries at the initial stages of GaN growth. Stacking faults have been observed near the GaN-sapphire interface and generally do not continue through the whole GaN film.[8] Open-core dislocations, also called nanopipes, run in the growth direction with a hexagonal cross section and $\{10\bar{1}0\}$ facets.[8–11] Qian *et al.*[11] identified the open-core dislocations as screw dislocations with a $[0001]$ Burgers vector. Inversion domains in GaN are similar to the open-core dislocations, but inside the $[0001]$ running cores is GaN of the opposite polarity.[10,12] V-defects in InGaN QWs are formed when threading dislocations intersect the QWs. They are inverted hexagonal pyramidal pits with $\{10\bar{1}1\}$ facets that open up to the InGaN top surface. When subsequent layers are grown on top of the InGaN layers, the pits fill in with the upper material.[13–18] Mg doped GaN with Ga polarity can have inverted hexagonal pyramid-shaped voids that have $(0001)$ top facets. Both $\{11\bar{2}2\}$ (Ref. 21) and $\{11\bar{2}3\}$ (Ref. 25) side facets have been reported. These voids are believed to form from Mg-rich clusters that are found just below the pyramid tip and cause the opening along Mg-decorated $\{11\bar{2}3\}$ planes. The polarity changes across these planes to the slower growing N polarity, which causes the void to form. Pyramid defect growth terminates when there is a lack of Mg on the defect walls and lateral overgrowth along the $(0001)$ planes is fast.[19–24]

Here, we report a GaN defect discovered using aberration-corrected scanning transmission electron microscopy (STEM). This defect consists of a hexagonal (0001) based pyramid void with $\{10\bar{1}1\}$ side facets and produces a dislocation along the [0001] growth direction, some of which are open core screw dislocations. STEM electron energy loss spectroscopy (EELS) reveals a large C concentration inside the voids and a larger C concentration below the void than above the void. We propose that the void defect is formed due to C deposition on the growth surface, which stops the GaN deposition locally. Dislocations at the pyramid void peaks are created from the imperfect meeting of the voids' six sidewalls.

## II. EXPERIMENTAL

We studied InGaN based GaN LED structures grown by vertical low-pressure MOCVD. Trimethylgallium (TMGa),

a)Author to whom correspondence should be addressed. Electronic mail: ayankovich@wisc.edu.

 

trimethylaluminum (TMAl), trimethylindium (TMIn), silane ($SiH_4$), $Cp_2Mg$, and ammonia ($NH_3$) were used as sources for Ga, Al, In, Si, Mg, and N, respectively. A ~3.7 $\mu$m *n*-type GaN template was grown on a c-plane sapphire substrate under a chamber pressure of 200 Torr at ~1000 °C. On top of the GaN template, the InGaN LED structure was grown. This started with ~1.5 $\mu$m of *n*-type GaN (Si doped, $n \approx 2\text{–}3 \times 10^{18}$ cm$^{-3}$) as a buffer layer grown under a chamber pressure of 150 Torr at ~1000 °C, followed by a multiple quantum well (MQW) structure consisting of ten 6 nm $In_{0.08}Ga_{0.92}N$ layers separated by 10 nm $In_{0.01}Ga_{0.99}N$ barriers. The MQW structure was topped with stair-case electron injector (SEI) layers consisting of 10 nm of $In_{0.04}Ga_{0.96}N$ and 10 nm of $In_{0.08}Ga_{0.92}N$. The MQW and SEI layers were *n*-type doped with Si to an electron density of $10^{18}$ cm$^{-3}$ and grown at 250 Torr and 700 °C. On top of the InGaN LED structures, a 10 nm thick *p*-type $Al_{0.15}Ga_{0.85}N$ layer was deposited to block electrons, followed by a 150 nm thick *p*-type Mg-doped GaN layer with a nominal hole density of $7 \times 10^{17}$ cm$^{-3}$ that was deposited at 950 °C and 150 Torr. Electrical, optical, and surface morphology properties also can be found elsewhere.[26–29]

We characterized the microstructure and defects of several LEDs using aberration-corrected STEM and STEM EELS spectrum imaging. Atomic resolution STEM utilizes a focused electron probe smaller than the diameter of an atom with a current large enough to produce meaningful signal at high angles in the diffraction plane. The STEM image is produced by scanning the probe across a thin sample, causing scattering of electrons to all angles. Electrons that are collected by a high angle annular detector produce a signal that depends strongly on the atomic number (Z) of the atoms under the beam and give this technique its names, high angle annular dark field (HAADF), and Z-contrast imaging.[30] In the simplest model, the intensity is proportional to $Z^{1.7}$, but in real experiments this is modified by dynamical diffraction[31] and strain.[32] If electrons are collected at smaller angles, diffraction contrast enters the image and sample strain is emphasized. Annular bright field (ABF) STEM is a recently discovered imaging technique, where only electrons in the outer annular region of the bright field zone are collected. ABF STEM allows the detection of light elements like in bright field STEM, but preserves the interpretability over thickness and defocus like Z-contrast STEM imaging.[33–36] We used high angle Z-contrast, smaller angle diffraction-contrast, and ABF STEM experiments. The spherical aberration corrector allows for partial correction of unavoidable lens aberrations, which on our STEM can produce $\leq$0.8 Å resolution Z-contrast images. STEM EELS measures the amount of energy the primary electrons lose due to inelastic scattering events while passing through the sample. The energy loss peaks are characteristic of the material's electronic structure and are therefore unique to the elements excited by the beam. EELS can be used to measure compositions, especially of light elements.

TEM samples were prepared using the mechanical wedge polish technique with diamond lapping films in the $[11\bar{2}0]$ cross-section and the [0001] plan-view projections. The samples were ion milled in a Fischione 1010 low angle ion mill and then in a Fischione low energy Nanomill. The Fischione 1010 ion mill parameters for both top and bottom ion guns in order were, (1) 4 kV and 5 mA at a 9° angle from the surface for one hour, and (2) 1.5 kV and 5 mA at a 9° angle from the surface for 15 min. The Fischione Nanomill parameters in order were, (1) 900 V and 115 pA at a 10° angle from the surface for 25 min, (2) 500 V and 115 pA at a 10° angle from the other surface for 25 mins, (3) 900 V and 115 pA at a −10° angle from the other surface for 25 mins, and (4) 500 V and 115 pA at a −10° angle from the surface for 25 mins. Immediately before the TEM experiments, samples were plasma cleaned in a Fischione plasma cleaner in 75% argon–25% oxygen mixture for 5 min to eliminate organic carbon surface contamination.

TEM bright field experiments were performed on a Phillips CM-200 microscope operated at 200 keV. STEM experiments were performed on a FEI Titan microscope with a CEOS probe aberration-corrector operated at 200 keV. HAADF STEM images were collected with a 24.5 mrad probe semi-angle, 24.5 pA probe current, and STEM resolution of 0.8 Å. By using a HAADF detector range of 54–270 mrad, diffraction contrast from elastic scattering was suppressed, leaving the images dominated by Z-contrast. By decreasing the detector collection angle range to 28.8–143.8 mrad in some images, more diffracted electrons were detected which caused enhanced strain contrast. ABF STEM images were collected simultaneously with HAADF STEM images, and therefore have the same probe conditions, but with an annular detector range of 11–24.1 mrad. STEM EELS spectrum images were acquired on the Titan using a 24.5 mrad probe semi-angle, 400 pA probe current, and STEM resolution of 2.1 Å. The EELS data were de-noised using principle component analysis implemented in HREM Research's MSA Digital Micrograph plug-in. The first 8 components were used in the spectrum images.

Although the Titan does not maintain ultrahigh vacuum at the sample (typical pressure is $7 \times 10^{-7}$ Torr), the microscope vacuum causes no measurable buildup of hydrocarbons on the sample. This was tested by scanning a pure silicon sample at 14 Mx (5.5 × 5.5 nm field of view) with a 100 pA probe continuously for 20 min, and measuring the EELS carbon K-edge every five minutes. There was no discernable carbon signal at the beginning of the test, and no discernable signal at the end of the test. We are therefore confident that carbon microanalysis and mapping in our STEM reflects the state of the sample, not the state of the microscope.

## III. RESULTS AND DISCUSSION

Figure 1 shows atomic resolution Z-contrast STEM images of a cross-section sample along the $[11\bar{2}0]$ zone axis. Figure 1(a) shows part of the *n*-type GaN, the whole InGaN QW structure, and *p*-GaN top layers with the [0001] growth direction pointing upwards in the image. Figure 1(a) shows small triangular shaped voids present in the *n*-type GaN and InGaN QW structure, but not in the Mg-doped *p*-GaN top layer. Similar voids were observed below the imaged area of Fig. 1(a), all the way through the *n*-type GaN and GaN template down to the sapphire/GaN interface, but not in the sapphire. The voids tend to form in similar {0001} planes

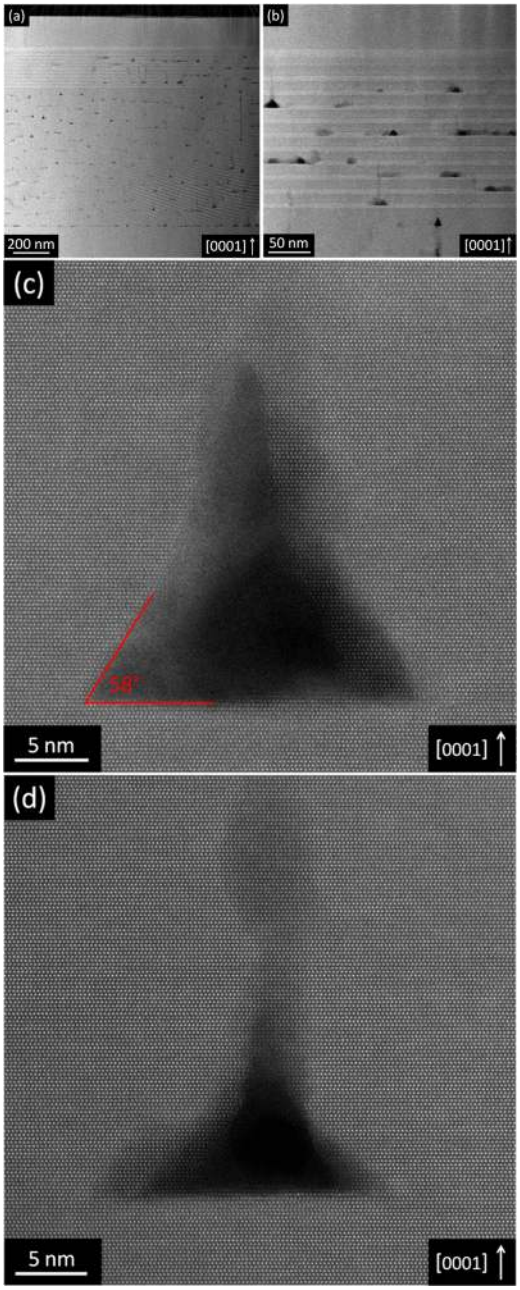


FIG. 1. (Color online) $[11\bar{2}0]$ Cross-section HAADF STEM images with the growth direction pointing up. (a) The GaN template, InGaN quantum well structure, and p-GaN top layers with voids present. (b) The InGaN quantum wells with voids present. (c) and (d) Two typical pyramid voids. The apparent fringes in the bottom right of (a) are Moiré fringes between the square STEM scan and the underlying crystal lattice.

perpendicular to the vertical growth direction in the images. Figure 1(b) is a higher magnification image of the QW structure showing the high In concentration layers as brighter bands due to the Z contrast. The voids in this region start at the same vertical position along the growth direction into the higher In concentration layers. Figure 1(c) is an atomic resolution STEM image showing a typical triangle void in the *n*-type GaN that has a sidewall angle of ~58° to the base. In all cases, the base plane of the voids is (0001). Typical sidewall angles range from 58° to 62° and void base lengths range from 5–75 nm, with a majority falling within the 5–25 nm range. The density of the voids greatly varies within each

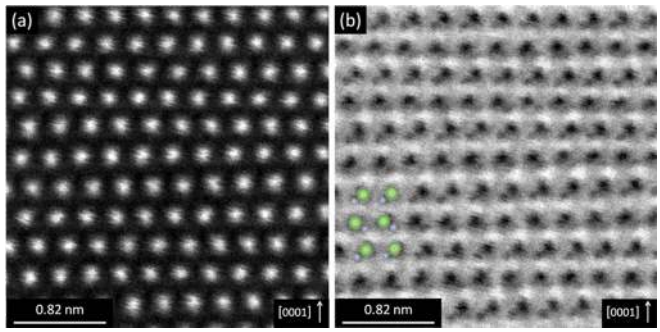


FIG. 2. (Color online) Simultaneously acquired (a) HAADF and (b) ABF $[11\bar{2}0]$ cross-section STEM images of GaN with the [0001] growth direction pointing up in the image, showing Ga polarity. A model of the Ga polarity atomic structure is shown in the inset of (b), with the larger green atoms being Ga and the smaller blue atoms being N.

sample, with some areas tens of square microns large having no voids while other areas may have up to $\sim 10^{15}$ cm$^{-3}$.

Figures 1(a) and 1(b) show that some triangular shaped voids have vertical nanopipe caps that extend hundreds of nanometers upward. Figure 1(d) shows a high resolution image of a typical triangle void with a vertical nanopipe cap. The lateral size of the nanopipe varies, but does not seem to grow larger than 10 nm.

Figure 2 shows simultaneously acquired (a) HAADF and (b) ABF $[11\bar{2}0]$ cross-section STEM images of GaN ([0001] growth direction pointing up in the image) within a sample that has a different set of InGaN layers than the LED structure in the other figures, but with the same substrate and template, and which also has pyramidal voids. The atomic column positions in the HAADF image of Fig. 2(a) represent the pure Ga columns, while the pure N columns are not visible due to the large Z difference between Ga and N and the Z-contrast nature of the image. In the ABF STEM image in Fig. 2(b), the pure Ga and pure N atomic columns are resolved and distinguishable. The Ga columns have a larger contrast than the N columns due to its larger Z number, and are therefore the upper atomic columns in the dumbbells. The Ga positions can also be determined by correlating the Ga positions in the HAADF STEM image in Fig. 2(a) to the atomic columns in the ABF image in Fig. 2(b), with the same result. ABF STEM imaging supplies an easily interpretable method to determine our samples have Ga polarity, as shown in the model superimposed on Fig. 2(b).

Figure 3 shows a TEM image (a) and STEM images (b-d) of a plan-view sample along the [0001] zone axis. The TEM image in Fig. 3(a) reveals hexagonal fringe contrast shapes with central contrast spots. The hexagonal fringe contrast shapes are Fresnel fringes, which arise due to diffraction from a sharp edge, and are characteristic of embedded voids.[37] This shows that the bases of the voids are all hexagons. The central contrast spots are characteristic of end-on dislocations, which form at the top tip of the void and propagate upwards along the growth direction. The extra background contrast in Fig. 3(a) is a result of thickness fringes and bend contours typical in TEM imaging. Figures 3(b)–3(d) are high resolution STEM images emphasizing strain/diffraction contrast, which enhances the visibility of the voids. At larger detector angle ranges, like those used in Fig. 1, the embedded

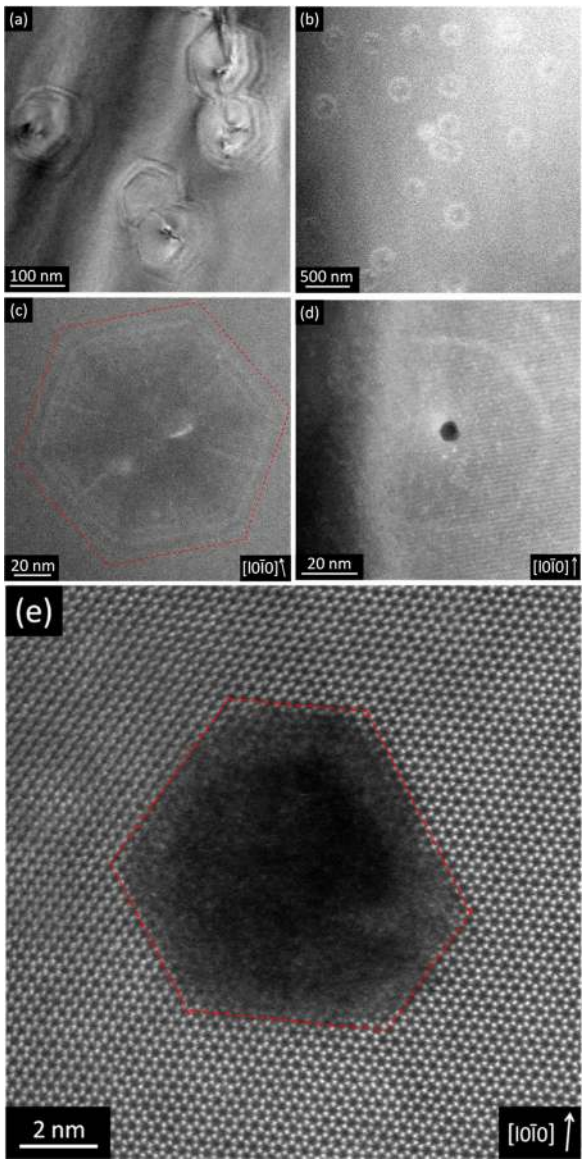


FIG. 3. (Color online) [0001] plan-view images. (a) TEM image showing Fresnel contrast from the embedded voids and central dislocation contrast. (b) STEM image showing Fresnel contrast from the embedded voids and central dislocation contrast. (c) and (d) Typical higher magnification STEM images of the embedded voids with the $\{10\bar{1}0\}$ facets labeled in (c). (e) High magnification STEM image of an open core dislocation cap.

voids in the plan-view samples are barely visible. Figure 3(b) again shows the hexagon Fresnel fringe contrast surrounding a central dislocation contrast spot. Figures 3(a) and 3(b) shows that all the hexagons are oriented with respect to one another, implying some crystallographic facet preference of the formation mechanism. Figure 3(c) shows a higher magnification [0001] projection image with $\{10\bar{1}0\}$ facets labeled in red showing the strain contrast and Fresnel fringes extending out from the void in a hexagonal shape, as well as the central strain contrast from the dislocation.

A Burgers vector circuit analysis was conducted on two atomic resolution images of closed dislocations, revealing the closed dislocations have a 1/3 $\langle 11\bar{2}0\rangle$ edge dislocation Burgers vector. This implies the closed dislocations are of either pure edge character or a mix of edge and screw character. Pure edge character would be consistent with known GaN threading dislocations.[7,8]

Figure 3(d) shows another [0001] projection of a void with a similar hexagonal contrast from the Fresnel fringes, but this time an open core dislocation has formed out of the top peak of the void. The open core dislocations are the vertical tube voids visible in Figs. 1(a), 1(b), and 1(d). Figure 3(e) is a high magnification Z-contrast STEM image that shows the same open core dislocation as in Fig. 3(d). The open core dislocations are hexagonal shaped with $\{10\bar{1}0\}$ facets. The size and crystallographic facets of the open core dislocations are consistent with previous reports.[9–11] A Burgers vector circuit analysis was conducted on two atomic resolution images of open dislocations, revealing the open core dislocations have no edge dislocation Burgers vector, implying they are purely screw dislocations. The facets of the open core dislocations are parallel to the facets of the hexagonal Fresnel contrast from the voids. This information, along with the knowledge that the side facets of the void are 58° to 62° from the (0001) bottom facet, reveal that the voids have $\{10\bar{1}1\}$ side facets. The Fresnel fringe contrast is always a nearly symmetric equal sided hexagon, while the open core dislocations are not always symmetric as seen in Fig. 3(e).

Figure 4 shows a schematic of the structure of these hexagonal-based pyramid voids. They all have symmetric hexagonal shaped (0001) base facets and $\{10\bar{1}1\}$ side facets. Each pyramid void has a dislocation at the peak of the pyramid, which extends up along the [0001] growth direction, as shown in Fig. 4(a). The dislocations sometimes glide laterally inside the (0001) planes within the GaN and the InGaN QWs. The closed dislocations have a 1/3 $\langle 11\bar{2}0\rangle$ Burgers vector component perpendicular to [0001], giving them at least some edge character. As shown in Fig. 4(b), some of the dislocations are hexagonal open core screw dislocations with $\{10\bar{1}0\}$ side facets, varying lateral widths, and varying degrees of hexagonal symmetry.

Figure 5 shows STEM EELS spectrum image data of a void viewed in cross-section. Figure 5(a) shows a STEM image of the InGaN layers with a hexagonal-based pyramid void where the spectrum image was taken. Figure 5(b) is the STEM image collected simultaneously with the EELS spectrum image. It is pixilated because the spectrum image pixel

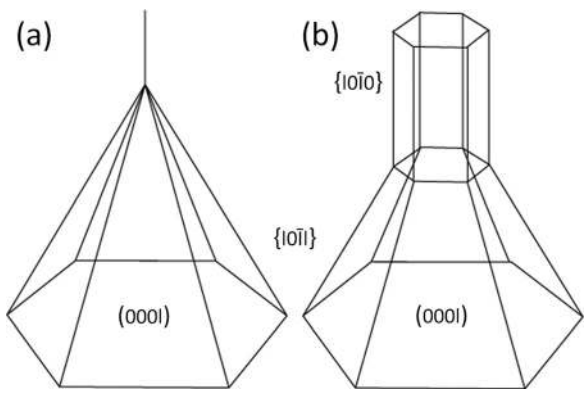


FIG. 4. Schematic diagrams showing the structure and facets of the hexagonal-based pyramid voids with (a) a dislocation cap and (b) an open core dislocation cap. The dislocation in (a) has some edge character, and the dislocation in (b) has none.

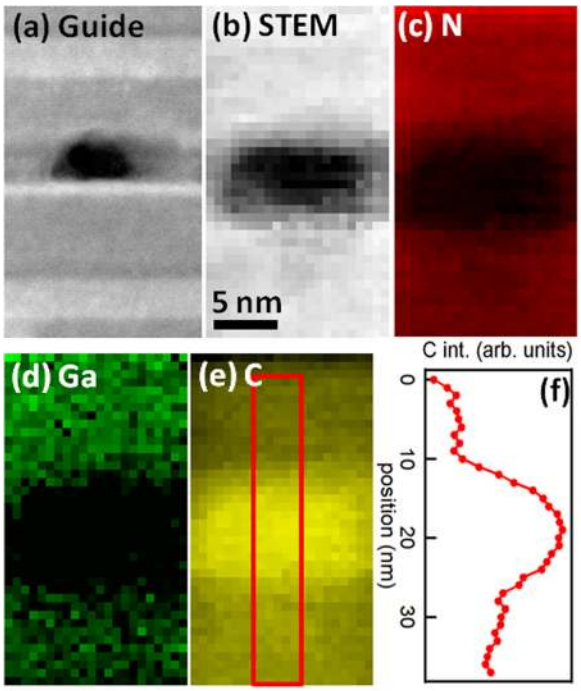


FIG. 5. (Color online) A STEM EELS spectrum image of a pyramid void. (a) HAADF STEM image of the sample area where the spectrum image was collected. (b) Simultaneous STEM image taken during the spectrum image. (c)-(e) are (c) nitrogen K, (d) gallium L, and (e) carbon K edge EELS intensity maps after background subtraction. (f) Horizontally integrated line profile of the red box in (e) showing the vertical carbon distribution across the void.

size was 0.664 nm/pixel, which is much larger than the STEM resolution. Figures 5(c)–5(e) are background-subtracted nitrogen K, gallium L, and carbon K edge EELS intensity maps, respectively, of the area shown in Fig. 5(b). Figure 5(f) is a horizontally integrated line profile of the red box in Fig. 5(e), showing the vertical carbon distribution across the void. Figures 5(e) and 5(f) indicate that there is a large C concentration inside or on the facets of the pyramid void, and that there is a larger C concentration below the void than above the void. This incorporated C may cause stress that contributes to the formation of the void and the capping dislocation. There is no indication that the sample is thicker under the void than above the void. Because carbon deposition is known to cause growth irregularities during deposition, we believe carbon contamination during the MOCVD deposition process acts as a growth mask and stops the GaN deposition locally. Subsequent layers of GaN are deposited around the C contaminated regions and the GaN begins to overhang the voided areas along the $\{10\bar{1}1\}$ facets until the voids are closed in from the top. The meeting of the six $\{10\bar{1}1\}$ facets at the pyramid's peak is not perfect, resulting in a dislocation.

This void is distinct from the V-defect found in InGaN QWs. The V-defect is not enclosed by a top plane, but instead is left open to the top surface until subsequent layers fill it. The void defect reported here is a fully enclosed void with a (0001) bottom facet. The V-defect initiates when a [0001] pointing dislocation created at the sapphire-GaN interface intersects the InGaN active region layers. The void reported in this paper does not initiate from a dislocation, but from C enriched regions and creates a [0001] pointing dislocation, which is not connected to the GaN/$Al_2O_3$ interface. V defects are only found in InGaN layers while the void reported here is found in InGaN and GaN layers, and V-defects are point down pyramids with respect to the growth direction while these defects are point up pyramids.

This void is also distinct from the inverted pyramidal defects found in Mg-doped GaN. Even though they are both found in Ga polarity GaN, the Mg-doped GaN defect initiates at the tip of the pyramid and therefore makes a point down pyramid with respect to the growth direction. The void defect reported here initiates with the (0001) facet as a basis and therefore produces a point up pyramid with respect to the growth direction. The pyramid defect previously reported has only been found in Mg and Be-doped GaN, while the defect reported here is found in GaN, Si-doped GaN, and InGaN. The sidewall facets of the Mg-doped GaN defect are $\{11\bar{2}3\}$, while the sidewall facets of this defect are predominantly $\{10\bar{1}1\}$. The pyramidal defects found in Mg-doped GaN are not associated with dislocations, while this defect produces a dislocation out the tip of the pyramid along [0001]. Finally, the Mg-doped GaN defect originates because of Mg rich clusters, while the defect presented here originates due to C deposition on the growth surface.

A layer of Mg-doped GaN with Mg concentrations in the range of $5 \times 10^{18}$ to $1 \times 10^{19}$ $cm^{-3}$ is the top layer of our LED structures. No defects like those previously reported by others in Mg-doped GaN were observed, which could be due to the higher Mg concentrations ($6 \times 10^{19}$ to $2 \times 10^{20}$ $cm^{-3}$) of the layers in which defects were observed.[21] In addition, no defect voids of the type reported here were found in the Mg-doped layer. This may be caused by increased lateral growth rate in Mg-doped GaN resulting in covering C-disturbed places with regular (0001) GaN.[38–40]

In-rich droplets can form during MOCVD growth due to the GaN/InGaN solid phase miscibility gap,[41,42] which could also cause voids. The voids reported here do not form by this mechanism because the voids do not only form in InGaN QWs, but also in nominally pure GaN that is grown in a different reactor from where the InGaN QWs are grown and in Si-doped *n*-GaN that is grown in the same reactor. Even in the InGaN, the voids are not associated with excess In, as shown in the Z-contrast images, which are essentially In maps in this system.

Voids with similar shapes, but much larger size have been created in GaN by utilizing a pattered under layer in an attempt to enhance light extraction in light emitting structures.[43] The voids presented here, if engineered correctly, could serve the same purpose and be easier to create. It might be possible to use a block-copolymer or self-assembled monolayer to create a structured carbon mask without lithography.

## IV. CONCLUSION

Using aberration-corrected STEM, we discovered a void defect in GaN and InGaN that is pyramid shaped with symmetric hexagonal shaped (0001) base facets and $\{10\bar{1}1\}$ side facets. Every pyramid void creates a dislocation from the top peak of the pyramid, which continues up along the [0001]

growth direction to the surface. Some of the dislocation caps form hexagonal open core screw dislocations with $\{10\bar{1}0\}$ side facets, varying lateral widths, and varying degrees of hexagon symmetry. Using STEM EELS spectrum imaging we discovered a large C concentration inside the pyramid void and a larger C concentration inside GaN below the void than above the void. We suggest that inadvertent carbon deposition during the MOCVD process acts as a growth mask and stops the GaN formation locally, creating the voided regions.

## ACKNOWLEDGMENTS

We acknowledge funding from the Department of Energy, Basic Energy Sciences (DE-FG02-08ER46547) and the Air Force Office of Scientific Research (FA9550-09-0447).

[1]S. Nakamura, M. Senoh, S. Nagahama, I. Naruhito, Y. Takao, T. Matsushita, Y. Sugimoto, and H. Kiyoku, Appl. Phys. Lett. **70**, 868870 (1997).
[2]S. J. Pearton, F. Ren, A. P. Zhang, and K. P. Lee, Mater. Sci. Eng. **R30**, 55 (2000).
[3]H. Morkoç, S. Strite, G. B. Gao, M. E. Lin, B. Sverdlov, and M. Burns, J. Appl. Phys. **76**, 1363 (1994).
[4]S. Nakamura, M. Senoh, S. Nagahama, N. Iwasa, T. Yamada, T. Matsushita, H. Kiyoku, and Y. Sugimoto, Jpn. J. Appl. Phys. **35**, L74 (1996).
[5]A. Michiue, T. Miyoshi, T. Yanamoto, T. Kozaki, S. I. Nagahama, Y. Narukawa, M. Sano, T. Yamada, and T. Mukai, Proc. SPIE **7216**, 72161Z (2009).
[6]W. Qian, M. Skowrinski, M. De Graef, K. Doverspike, L. B. Rowland, and D. K. Gaskill, Appl. Phys. Lett. **66**, 1252 (1994).
[7]R. C. Powell, N. E. Lee, Y. W. Kim, and J. E. Greene, J. Appl. Phys. **73**, 189 (1993).
[8]P. Vennegues, B. Beaumont, M. Vaille, and P. Gibart, J. Cryst. Growth **173**, 249 (1997).
[9]P. Vennegues, B. Beaumont, M. Vaille, and P. Gibart, Appl. Phys. Lett. **70**, 2434 (1997).
[10]Z. Liliental-Weber, Y. Chen, S. Ruvimov, and J. Washburn, Mater. Sci. Forum **258–263**, 1659 (1997).
[11]W. Qian, G. S. Rohrer, M. Skowronski, K. Doverspike, L. B. Rowland, and D. K. Gaskill, Appl. Phys. Lett. **67**, 2284 (1995).
[12]J. L. Rouviere, M. Arley, R. Niebuhr, K. H. Bachem, and O. Briot, Mat Sci and Eng B **43**, 161 (1997).
[13]X. H. Wu, C. R. Elsass, A. Abare, M. Mack, S. Keller, P. M. Petroff, S. P. DenBaars, and J. S. Speck, Appl. Phys. Lett. **72**, 692 (1998).
[14]Y. Chen, H. Takeuchi, H. Amano, I. Akasaki, N. Yamada, Y. Kaneko, and S. Y. Wang, Appl. Phys. Lett **72**, 710 (1998).
[15]I. Kim, H. Park, Y. Park, and T. Kim, Appl. Phys. Lett. **73**, 1634 (1998).
[16]J. Off, F. Scholz, E. Fehrenbacher, O. Gfrorer, A. Hangleiter, G. Brockt, and H. Lakner, Phys. Status Solidi B **216**, 529 (1999).
[17]K. Watanabe, J. R. Yang, S. Y. Huang, K. Inoke, J. T. Hsu, R. C. Tu, T. Yamazaki, N. Nakanishi, and M. Shiojiri, Appl. Phys. Lett. **82**, 718 (2003).
[18]A. M. Sanchez, M. Gass, A. J. Papworth, P. J. Goodhew, P. Singh, P. Ruterana, H. K. Cho, R. J. Choi, and H. J. Lee, Thin Solid Films **479**, 316 (2005).
[19]P. Vennegues, M. Benaissa, S. Dalmasso, M. Leroux, E. Feltin, P. De Mierry, B. Beaumont, B. Damilano, N. Grandjean, and P. Gibart, Mater. Sci. Eng. **B93**, 224 (2002).
[20]P. Vennegues, M. Leroux, S. Dalmasso, M. Benaissa, P. De Mierry, P. Lorenzini, B. Damilano, B. Beaumont, J. Massies, and P. Gibart, Phys. Rev. B **68**, 235214 (2003).
[21]Z. Liliental-Weber, M. Benamara, W. Swider, J. Washburn, I. Grzegory, S. Porowski, R. D. Dupuis, and C. J. Eiting, Physica B, **273–274**, 124 (1999).
[22]Z. Liliental-Weber, M. Benamara, W. Swider, J. Washburn, I. Grzegory, S. Porowski, D. J. H. Lambert, C. J. Eiting, and R. D. Dupuis, Appl. Phys. Lett. **75**, 26 (1999).
[23]Z. Liliental-Weber, J. Jasinski, M. Benamara, I. Grzegory, S. Porowski, D. J. H. Lambert, C. J. Eiting, and R. D. Dupuis, Phys. Status Solidi B **228**, 345 (2001).
[24]Z. Liliental-Weber, T. Tomaszewicz, D. Zakharov, J. Jasinski, and M. A. O'Keefe, Phys. Rev. Lett. **93**, 20 (2004).
[25]J. Xie, Ü. Özgür, Y. Fu, X. Ni, H. Morkoç, C. K. Inoki, T. S. Kuan, J. V. Foreman, and H. O. Everitt, Appl. Phys. Lett. **90**, 4 41107-1-3 (2007).
[26]X. Li, F. Zhang, S. Okur, V. Avrutin, S. J. Liu, Ü. Özgür, H. Morkoç, S. M. Hong, S. H. Yen, and T. S. Hsu, Phys. Status Solidi A **208**, 2907 (2011).
[27]X. Ni, X. Li, J. Lee, S. Liu, V. Avrutin, Ü. Özgür, H. Morkoç, and A. Matulionis, Appl. Phys. Lett. **97**, 031110 (2010).
[28]X. Li, H. Y. Liu, S. Liu, X. Ni, M. Wu, V. Avrutin, N. Izyumskaya, Ü. Özgür, and H. Morkoç, Phys. Status Solidi A **207**, 1993 (2010).
[29]H. Y. Liu, X. Li, X. Ni, M. Wu, V. Avrutin, N. Izyumskaya, Ü. Özgür, A. B. Yankovich, A. V. Kvit, P. M. Voyles, *et al.*, Phys. Status Solidi C **8**, 1548 (2011).
[30]S. J. Pennycook, Annu. Rev. Mater. Sci. **22**, 171 (1992).
[31]S. E. Hillyard, R. F. Loane, and J. Silcox, Ultramicroscopy **49**, 14 (1993).
[32]D. D. Perovic, C. J. Rossow, and A. Howie, Ultramicroscopy **52**, 353 (1993).
[33]E. Okunishi, I. Ishikawa, H. Sawada, F. Hosokawa, M. Hori, and Y. Kondo, Microsc. Microanal. **15**(2), 164 (2009).
[34]S. D. Findlay, N. Shibata, H. Sawada, E. Okunishi, Y. Kondo, T. Yamamoto, and Y. Ikuhara, Appl. Phys. Lett. **95**, 191913 (2009).
[35]S. D. Findlay, N. Shibata, H. Sawada, E. Okunishi, Y. Kondo, S. Azuma, and Y. Ikuhara, Microsc. Microanal. **16**(2), 80 (2010).
[36]S. D. Findlay, N. Shibata, H. Sawada, E. Okunishi, Y. Kondo, and Y. Ikuhara, Ultramicroscopy **110**, 903 (2010).
[37]M. Ruhle and M. Wilkens, Cryst. Lattice Defects **6**, 129 (1975).
[38]S. Haffouz, B. Beaumont, and P. Gibart, MRS Internet J. Nitride Semicond. Res. **3**, 8 (1998).
[39]B. Beaumont, V. Bousquet, P. Vennegues, M. Vaille, A. Bouille, P. Gibart, S. Dassonneville, A. Amokrane, and B. Sieber, Phys. Status Solidi A **176**, 567 (1999).
[40]P. Gibart, Rep. Prog. Phys. **67**, 667 (2004).
[41]I.-H. Ho and G. B. Stringfellow, Appl. Phys. Lett. **69**, 2701 (1996).
[42]A. Wakahara, T. Tokuda, X.-Z. Dang, S. Noda, and A. Sasaki, Appl. Phys. Lett. **71**, 906 (1997).
[43]M. Ali, A. E. Romanov, S. Suihkonen, O. Svensk, P. T. Torma, M. Sopanen, H. Lipsanen, M. A. Odnoblyudov, and V. E. Bougrov, J. Cryst. Growth **315**, 188 (2011).